

Efficient solar light photocatalytic degradation of commercial pharmaceutical drug and dye using rGO-PANI assisted c-ZnO heterojunction nanocomposites



Edugulla Girija Shankar ^{b,c}, Mallelakari Aishwarya ^b, Anas Khan ^b, A.B.V. Kiran Kumar ^{a,b,*},
Jae Su Yu ^{c,**}

^a Vijaya Lab, Buchireddypalem, Nellore District, Andhra Pradesh, 524305, India

^b Amity Institute of Nanotechnology, Amity University, Noida, U.P, 201313, India

^c Department of Electronics and Information Convergence Engineering, Institute for Wearable Convergence Electronics, Kyung Hee University, Yongin-si, Gyeonggi-do, 17104, Republic of Korea

ARTICLE INFO

Keywords:

Natural sunlight photocatalysis
Amoxicillin and clavulanate potassium
Methylene blue dye
Ternary nanocomposite
Exciton lifetime
Doping
Water purification

ABSTRACT

The major requirement of a solar light-activated photocatalyst is the effective utilization of the light-induced electron-hole pair and exciton lifetime. Herein, the reduced graphene oxide and polyaniline assisted carbon doped porous ZnO (c-ZnO) heterojunction nanocomposites (RPZ nanocomposites) were designed for enhanced photocatalytic degradation of the commercially available pharmaceutical antibiotic drug amoxicillin and clavulanate potassium (ACP) and methylene blue (MB) dye using natural sunlight. The surface morphology, phase purity, and bonding environment of the prepared RPZ heterojunction nanocomposite were analyzed using scanning electron microscopy, X-ray diffraction, and soft X-ray absorption spectroscopy, respectively. In comparison with pure ZnO, a doping and composite formation reduced the bandgap energy from 3.34 to 2.80 eV, calculated using the Tauc plot. From photocatalytic degradation studies, the as-prepared RPZ heterojunction nanocomposite efficiently degraded 95% and 47% of MB dye and ACP in 100 min under natural sunlight with the reaction rates of 0.0296 and 0.0055 min⁻¹, respectively. The removal efficiency of the photocatalyst was obtained to be 95% and 46.14% for MB dye and ACP, respectively.

1. Introduction

Over the years, water pollution is a major concern across the world. The release of untreated effluents from the industries such as pharmaceuticals, textile, and leather is one of the major contributors to water pollution. The pharmaceutical and textile industrial effluents contain the compounds such as azo dyes and toxic organic compounds. The presence of the following compounds in the water body can hazard the aquatic life. Precisely, antibiotics are one of the major class of pharmaceutical drug materials, and the presence of these compounds in the pharmaceutical industrial effluents can hazard the aquatic life and humans. The antibiotic compounds may enter the freshwater environments by the release of untreated effluents from pharmaceutical industries, other medical facilities, and hospitals. These compounds in groundwater, sewage effluent, and drinking water may cause

genotoxicity in aquatic organisms, affecting non-targeted organisms and human pathogens [1]. Among the pharmaceutical compounds, antibiotics have an important role in the contamination of the water due to the high consumption rate through both human and veterinary medicine. Moreover, even low concentrations of antibiotics in the environment increase the development of the antibiotic-resistant bacterial known as multi-drug resistant (MDR) bacterial strains [2]. Many researchers have reported that the increase in the MDR strains is due to the existing antibiotics in wastewater which are released from industries in the water source [3].

The removal of the following toxins (azo dyes and antibiotics) is extremely problematic due to the high solubility and stability of following in water. Over the past years, many water purification technologies have been developed for the treatment of medicine and textile-related industrial effluents such as reverse osmosis, activated carbon (C)

* Corresponding author. Vijaya Lab, Buchireddypalem, Nellore District, Andhra Pradesh, 524305, India

** Corresponding author.

E-mail addresses: bharanichem@gmail.com (A.B.V.K. Kumar), jsyu@khu.ac.kr (J.S. Yu).

absorption, air stripping, centrifugation, flocculation, and biological treatment. However, the main drawback of these purification techniques is that all these processes convert pollutants from one phase to another phase, causing the production of secondary pollutants [4] and biological treatment is limited to biodegradable compounds only. For this reason, solar light photocatalysis has emerged as the most promising and safe effluent treatment technique because this uses an advanced oxidation process to generate reactive oxygen species (ROS) such as hydroxyl radicals (OH^{\cdot}) and superoxide radicals (O_2^{\cdot}) which degrade the pollutants into safe by-products of CO_2 and H_2O . Sunlight, i.e., an abundant, clean, and economical source of light energy, is used as an initiation energy for the generation of ROS.

Semiconductor-based photocatalysis has attracted great attention for the degradation of environmental pollutants like pharmaceutical compounds such as amoxicillin, ampicillin, ciprofloxacin, and cloxacillin antibiotics [5] as well as toxic dyes including methylene blue, methyl orange, and Rhodamine B in water [6,7]. The most studied semiconductor material for photocatalysis applications is titanium dioxide (TiO_2) and zinc oxide (ZnO) nanoparticles due to advantageous properties like tunable bandgap, thermal stability, biocompatibility, and ultraviolet (UV) absorption. But, drawbacks such as wide bandgap (3.37 eV) and low exciton time have suppressed photocatalytic degradation efficiency of the following.

In this regard, heterojunction nanocomposites with various dopants have appeared as the most promising photocatalyst material with activation energy lying in the visible wavelength region and high exciton time due to charge transfer. The generation of ROS is directly proportional to the exciton lifetime. Few of the reported heterojunction nanocomposites are Fe_3O_4 -graphene oxide, silver iodide/g-C₃N₄, CuFeNLDH-CNTs, Gd₂ZnMnO₆/ZnO, TbFeO³, biochar-ZnO, and CaMgO₂ [8–14]. However, previous publications report the photocatalytic degradation of purified (analytical grade) pharmaceutical compounds, but pharmaceutical compounds used in the pharmaceutical industry contain more complex compound structure and higher concentration compared to analytical grade compounds. In this regard, reduced graphene oxide (rGO) and polyaniline (PANI) assisted C doped porous ZnO (c-ZnO) (RPZ) heterojunction nanocomposite was synthesized for photocatalytic degradation of novel commercially available amoxicillin and clavulanate potassium (ACP) and methylene blue (MB) dye in the present investigation.

The rGO with a two-dimensional (2D) layer provides excellent electron transportation property. Graphene has been extensively studied for applications in catalysis, hydrogen storage, solar cells, and batteries. Moreover, graphene has a potential application in photocatalysis due to its ability to accept electrons, enhancing the recombination time. In addition, favorable adsorption properties due to the conjugation between the dye molecule and aromatic rings in graphene further promote the catalyst activity. Besides, PANI owing to the high mobility of charge carriers has gained attraction in applications including light-emitting diodes, supercapacitors, corrosion protective paints, and particularly photocatalysis. Under visible light irradiation, PANI acts as an excellent acceptor of holes, resulting in enhanced photocatalytic activity [15]. Moreover, the carboxylic acid functional groups in rGO have strong interaction with PANI and ZnO nanoparticles, resulting in strong adsorption of ZnO and PANI on rGO [16]. The following interaction enhances the long-term durability and reproducibility of photocatalyst. In the current investigation, RPZ heterojunction nanocomposite was synthesized and employed for solar light photocatalytic water splitting for the degradation of ACP in water purification application, and further used for characterization.

2. Experimental section

2.1. Materials and methods

Zinc acetate dihydrate ($\geq 98\%$), poly (vinyl alcohol) (PVA, 99%, Mw

89,000–98,000), aniline ($\geq 99.5\%$), hydrochloric acid (37%), ammonium persulfate ($\geq 98\%$), graphite flakes (99%), sulfuric acid (98%), sodium nitrate ($\geq 99\%$), potassium permanganate ($\geq 99\%$), and hydrogen peroxide were purchased from Sigma Aldrich Co., South Korea. Distilled (DI) water with a resistivity of 18.25 MΩ and ethanol ($\geq 99.5\%$) were used for the experiments.

2.1.1. Synthesis of c-ZnO

The c-ZnO was synthesized using a two-step facile thermal decomposition method. First, 1 g of zinc acetate dihydrate and 10 wt% PVA were dissolved in 1:1 of DI water and ethanol solution using magnetic stirring. The stirring was continued until a clear solution was obtained. The PVA and c-ZnO complex blend was heated at 100 °C for 12 h in an oven. Second, the obtained complex blend was annealed at three different temperatures of 300, 400, and 500 °C in a muffle furnace at a ramp temperature of 5 °C/min for 2 h.

2.1.2. Synthesis of rGO

The rGO was prepared using the modified Hummer's method. Firstly, 3 g and 1.5 g of graphite flakes and sodium nitrate, respectively were added in 150 mL of concentrate sulfuric acid under constant stirring. Then, the solution was transferred to an ice bath. 8 g of potassium permanganate was added to the above solution very slowly for 4 h. 100 mL of DI water was added slowly to the above solution and kept for stirring at 95 °C for 12 h. Afterward, 30 mL of hydrogen peroxide was added to the obtained solution. The obtained suspension was centrifuged at 3000 rpm, washed using 1 M hydrochloric acid (HCl) and DI water, and kept for drying at 80 °C for 12 h. The obtained black powder was named as rGO.

2.1.3. Synthesis of RPZ heterojunction nanocomposite

Initially, 1:1 rGO and c-ZnO were ground finely for 30 min. In this facile synthesis method, aniline was used as a monomer for PANI synthesis. Aniline and HCl were taken in a 1:1 ratio and the mixture was stirred for 30 min at room temperature. Furthermore, finely ground rGO and c-ZnO were added and the stirring was continued for 30 min. The obtained mixture was transferred into an ice bath and 1 M APS (Ammonium Persulfate) solution was added dropwise under continuous stirring. Initially, magenta color was observed, and the reaction was further continued until emeraldine green color was obtained. An obtained complex was washed using DI water and ethanol, kept for drying at 60 °C for overnight. The same reactions were performed for three c-ZnO samples and the obtained compounds were named as RPZ-300, RPZ-400, and RPZ-500. Fig. 1(a) shows the schematic representation of the RPZ heterojunction nanocomposite synthesis.

2.2. Characterization

Field-emission scanning electron microscope (FE-SEM, Merlin Carl Zeiss, South Korea) was employed to study the surface morphology of the nanocomposite. To understand the crystal structure of the nanocomposite, powder X-Ray diffraction (XRD, Cu K α , D8 Advance, Bruker, South Korea) studies were performed at a scan rate of 4° per min with the 2θ scan range from 10° to 80°. Synchrotron-based soft X-ray absorption spectroscopy (SXAS) studies were performed for elemental analysis and bonding environment of nanocomposite in total electron yield (TEY) mode at Beamline 01, INDUS 2, RRCAT, India. UV-Vis-NIR spectrophotometer (UV-2600, Shimadzu, South Korea) was used to perform UV-VIS diffusive reflectance studies with a scan range from 200 to 800 nm.

2.3. ACP extraction and photocatalytic activity

As a penicillin family of antibiotics, ACP tablet which is commercially available from Abbott Healthcare Pvt. Ltd. was used. ACP was extracted from the tablet using the mechanical shaking method.

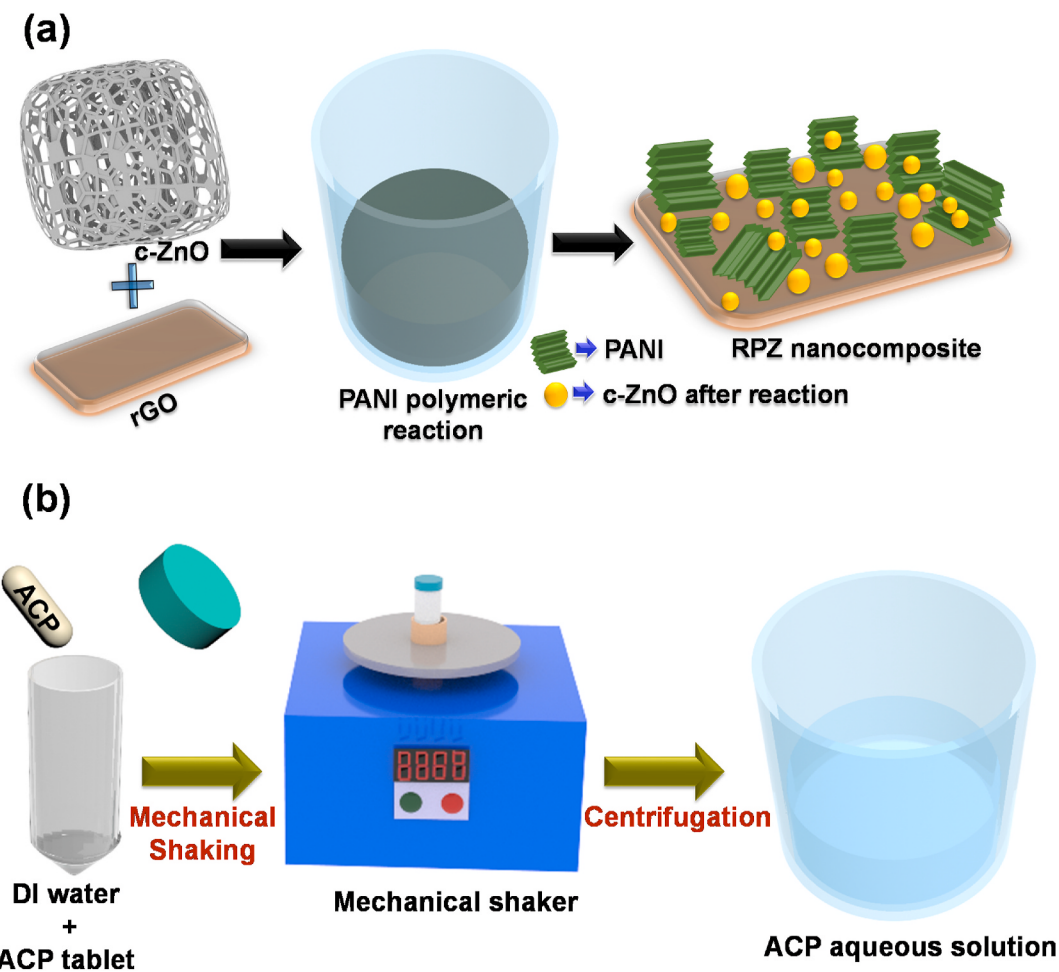


Fig. 1. (a) Schematic representation for the synthesis of RPZ heterojunction nanocomposite, and (b) schematic representation of the ACP aqueous solution extraction from the tablet.

Initially, net content 650 mg ACP tablet was added to 10 mL DI water in a centrifuge tube and placed in a mechanical shaker. Here, the shaking was performed for 6 h at 1000 rpm. The obtained solution was centrifuged and passed through the Whatman filter paper. The obtained transparent solution was 0.17 M ACP dissolved stock solution. This stock solution was further used for photocatalytic degradation analysis. Fig. 1(b) shows the schematic representation of ACP extraction from the tablet.

Photocatalytic degradation efficiency of the synthesized RPZ heterojunction nanocomposites against ACP was measured under direct sunlight in Yongin-Si, Republic of Korea with Latitude: 37.2411° N Longitude: 127.1776° E Elevation above sea level: 430 ft. Three different degradation solutions were prepared by adding 2 mL of 0.17 M stock solution of ACP to 48 mL DI water and the 0.1 g RPZ-300, RPZ-400, and RPZ-500 were added to the respective solution. For reference, 10 ppm MB dye solution was used for degradation. Initially, 3 mL of the samples was collected from each degradation solution before irradiating the sunlight and the rest of the samples was collected at the interval of 20 min for the next 100 min from each solution. Thereafter, the collected samples were analyzed using a UV-Vis spectrophotometer with a scan range of 200–800 nm.

3. Results and discussion

The photocatalytic efficiency can be enhanced by tuning the bandgap and morphology and by increasing the recombination time through the formation of heterojunction nanostructure with doping. In

the present investigation, the RPZ heterojunction nanocomposite is designed as a doped heterojunction with an interface between the PANI and c-ZnO, whereas the rGO at the interface of PANI/c-ZnO acts as an electron scavenger. The following ternary interface increased the recombination time, causing the enhanced and efficient photocatalytic degradation of the ACP. As shown in the schematic of Fig. 1(a), the PANI flakes and c-ZnO nanoparticles were decorated on the rGO sheets as can be seen in the FE-SEM images (Fig. 2). The doping and interface interaction were analyzed using XRD and SXAS studies.

Fig. 2 illustrates the FE-SEM images of the c-ZnO, rGO, and RPZ heterojunction nanocomposite. Fig. 2(a) depicts the interconnected spherical c-ZnO nanoparticles, leading to the formation of a porous nanostructure. Fig. 2(b) shows the formation of the nanosheets of rGO. The PANI flakes and c-ZnO nanoparticles were decorated on the rGO nanosheets (Fig. 2(c) and (d)). The interconnected c-ZnO nanoparticle was fractured into individual nanoparticles due to physical grinding. Furthermore, the carboxylic acid functional groups in rGO have strong interaction with PANI flakes and c-ZnO nanoparticles, causing high absorption on the rGO nanosheets, as can be observed in the FE-SEM images [16]. The uniformly distributed PANI and c-ZnO on the surface of the rGO nanosheets further enhance the heterojunction photocatalytic degradation efficiency and cyclic stability of RPZ nanocomposite.

XRD studies were performed to investigate the crystal structure and composite formation of the as-prepared nanocomposites. Fig. 3(a)–(d) shows the XRD patterns of pure ZnO, RPZ-300, RPZ-400, and RPZ-500, respectively. The XRD patterns of all the prepared RPZ heterojunction

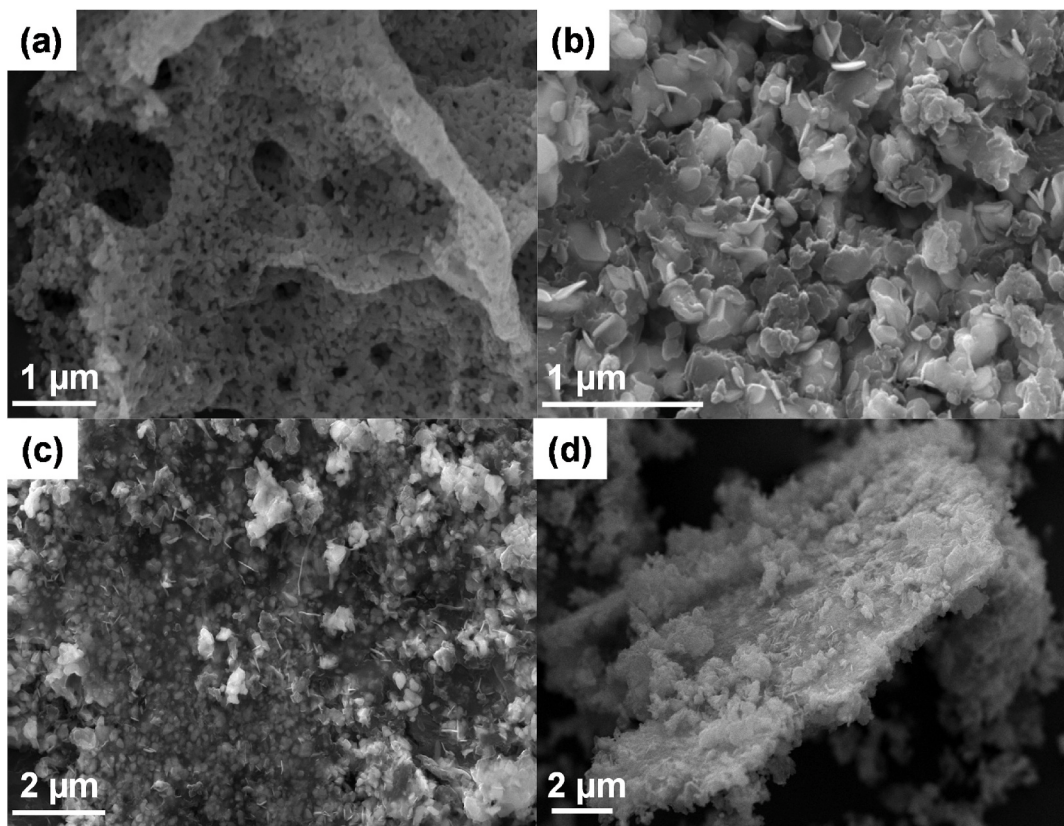


Fig. 2. FE-SEM images of (a) c-ZnO, (b) rGO, and (c,d) c-ZnO and PANI decorated rGO sheets (RPZ heterojunction nanocomposite).

nanocomposites were similar. The characteristic peaks of c-ZnO were exactly matched with the hexagonal wurtzite ZnO structure and the peak indexing was done corresponding to the (100), (002), (102), (110), (103), (200), (112), (201), (004), and (202) planes [17]. The additional peaks were observed at $2\theta = \sim 15^\circ$ and 23° corresponding to the PANI oriented in the (121) and (113) planes, respectively [18]. Peak width and intensity correspond to the PANI polymer chain degree of orientation and crystallite population in the following plane, respectively [19]. Maximum intensity was observed at the peak corresponding to the (113) plane. The separation length (R) was 5.2374 \AA , calculated for the highest intensity PANI (113) peak using the following equation given by the Klug and Alexander [19]:

$$R = 5\lambda/8\sin\theta \quad (1)$$

The broad hump at $2\theta = \sim 25^\circ$ corresponds to the rGO oriented in a (002) plane [18]. The broad peak corresponds to the formation of a few monolayers of rGO sheets [20]. The following results confirm the presence of PANI and rGO phases in the prepared nanocomposite. Lattice parameters (a and c), d spacing (d), volume (Vol), and full width at half maximum (FWHM) (β) were calculated, and crystallite size (D) using Scherer's formula was calculated using Eq. (2) for the (101) peak and listed in Table 1 [21].

$$a = \lambda/\sqrt{3} \sin\theta; c = \lambda/\sin\theta; d = n\lambda/2\sin\theta; \text{Vol} = (\sqrt{3}/2) \times a^2 c; D = k\lambda/\beta_{hkl} \cos\theta \quad (2)$$

From the XRD diffraction peaks, lattice parameters, a and c , were calculated using the highest intensity (101) peak for as-prepared nanocomposite and compared with pure ZnO. Table 1 depicts the increase in the values of lattice parameters, spacing, and volume for the prepared nanocomposite when compared to the pure ZnO. This may be caused by the substitution doping of the C atom in the ZnO crystal structure, as the ionic radius of the C is higher as compared to oxygen [22]. The substitution of C will lead to tensile stress on the ZnO crystal lattice, causing an

expansion of crystal grain size [23]. Here, PVA and zinc acetate dihydrate will act as a C source at higher temperatures. Furthermore, the change in the FWHM was observed for the prepared nanocomposite compared to the pure ZnO which is another evidence of C doping in the ZnO lattice structure.

The formation of the rGO-PANI-c-ZnO ternary doped heterojunction nanocomposite can be confirmed from the XRD patterns of the prepared nanocomposites and pure ZnO. Further SXAS studies were performed to analyze the formation of the nanocomposites and interface among the different phases in a nanocomposite. To understand the elemental mapping, chemical environment, and interactions inside the prepared RPZ heterojunction nanocomposite, synchrotron-based SXAS studies were performed. Fig. 4 shows the C K-edge, O K-edge, N K-edge, and Zn L-edge SXAS spectra of RPZ-300, RPZ-400, and RPZ-500 nanocomposites, which further confirms the presence of PANI, rGO, c-ZnO, and C as a dopant in the prepared RPZ heterojunction nanocomposite as observed in the XRD analysis. Fig. 4(a) shows the SXAS C K-edge spectra of RPZ-300, RPZ-400, and RPZ-500 nanocomposites, which provides the C elemental mapping in the prepared nanocomposites. The peak A at 285 eV indicates the presence of C=C ring structures corresponding to the 1s- π^* transition of aromatic/olefinic carbon. This is attributed to the transition of electrons from C 1s to unoccupied states of C=C π^* , further confirming the presence of rGO in the prepared nanocomposites as revealed in XRD patterns [24]. The intensity of peak A corresponds to an unoccupied density of state (DOS) of the π^* character. As reported in the literature, peak A is evidence of the charge transfer from c-ZnO structure to C 2p derived π^* states in rGO at the interface of c-ZnO/rGO [25]. The peak B at 286 eV corresponds to the 1s- π^* transition of vinyl-keto (C=C-C=O). The peak C at 288 eV is related to the C atom of rGO attached to the O and other atoms, which is attributed to the formation of the C-O-Zn-PANI interface in the prepared RPZ heterojunction nanocomposites [26]. The peak D at 291 eV corresponds to the σ^* C-C transitions [17]. Fig. 4(b) shows the O K-edge SXAS spectrum of the

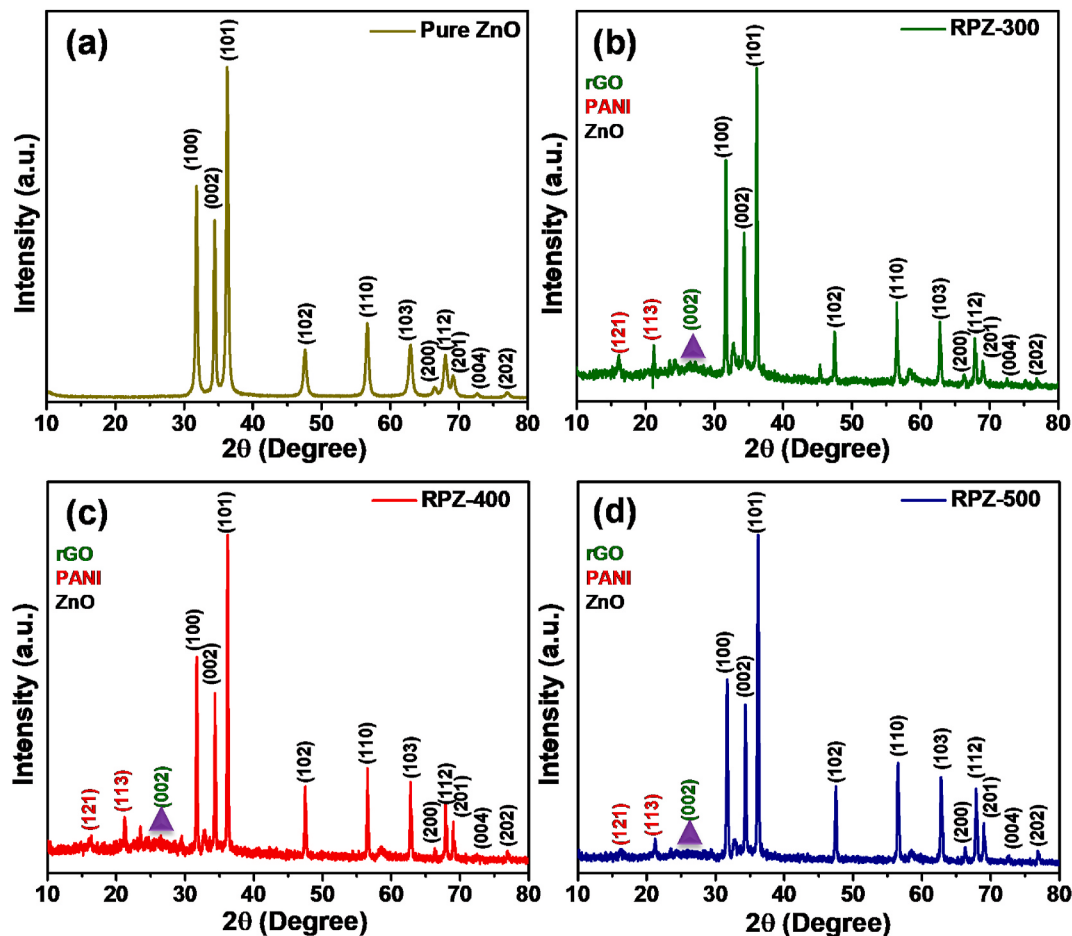


Fig. 3. XRD patterns of (a) pure ZnO, (b) RPZ-300, (c) RPZ-400, and (d) RPZ-500.

Table 1

Lattice parameters, spacing, volume, and FWHM of pure ZnO, RPZ-300, RPZ-400, and RPZ-500.

Sample name	a (Å)	c (Å)	d (Å) (d spacing)	D (nm)	β (°)	Vol (Å³)
Pure ZnO	2.855872	4.94677	0.251379355	25.71	0.33983	34.94034
RPZ-300	2.862013	4.957408	0.252135137	41.81	0.20893	35.16623
RPZ-400	2.864747	4.962142	0.251902349	39.47	0.22132	35.26708
RPZ-500	2.862892	4.958929	0.251977157	35.14	0.24862	35.19862

prepared nanocomposites and it was compared with the pure ZnO. The four main characteristic absorption peaks were observed between the 530–550 eV, named as A, B, C, and D accordingly. The absorption peaks correspond to the charge transition from O core 1s to 2p. In general, the peak A at 533 eV appears due to the formation of molecular orbital between O 2p and incomplete 3d orbital in metals. Due to the completely filled 3d orbitals in Zn, no significant absorption can be observed from Fig. 5(b) for peak A. The main significant absorption was observed for peak B at 537 eV corresponding to the hybridization between O 2p and Zn 4s orbitals. The peaks C and D at 537 and 540 eV, respectively occurred due to the interaction between O 2p and Zn 4p orbitals [27]. Fig. 4(c) shows the N K-edge SXAS spectra which confirm the presence of the N element in all the prepared RPZ heterojunction nanocomposites. The three significant peaks were observed at the energy between 400 and 410 eV. The following peaks correspond to the interactions of unoccupied N 2p orbitals with ion states. The peak A is attributed to the Zn–N interaction due to the charge transition from the N 1s to Zn 3d–4s orbitals. The peaks B and C correspond to the 1s to π^* transitions. This further confirms the presence of the PANI in the

prepared RPZ heterojunction nanocomposites as observed in the XRD patterns [24]. Fig. 4(d) shows the Zn L2, L3-edge SXAS spectra of the prepared RPZ heterojunction nanocomposites in comparison with the pure ZnO. The L-edge spectra of the transition metal are very sensitive to adjacent atom environment and electronic state of atoms. The Zn L-edge SXAS absorption spectra arise due to the charge transitions from the 2p_{3/2} and 2p_{1/2} to the unoccupied 4s and 4d orbitals. The Zn L2, L3-edge SXAS spectra are ascribed to the formation of molecular orbitals, due to the overlapping of 3d and 4p orbitals. The peaks A, B, and C correspond to the Zn L3 edge whereas the peak D corresponds to the Zn L2 edge. The peak A at 1020 eV appears due to the low energy level caused by the asymmetry in the wurtzite ZnO structure, and it is also known as a pre-edge peak. The Zn 2p_{3/2}–4s absorption peak A at 1020 eV is similar as explained in the O K-edge SXAS spectra, which is due to the hybridization of O 2p and Zn 4s orbitals. The peaks after 1025 eV are due to the Zn 4d transition. Further O K-edge and Zn L-edge SXAS analyses are angle-dependent due to the bilayer bonding along the c axis-oriented bond. The intensity in Zn L-edge SXAS peaks is related to the unoccupied DOS. The changed peak intensity of both O K-edge and

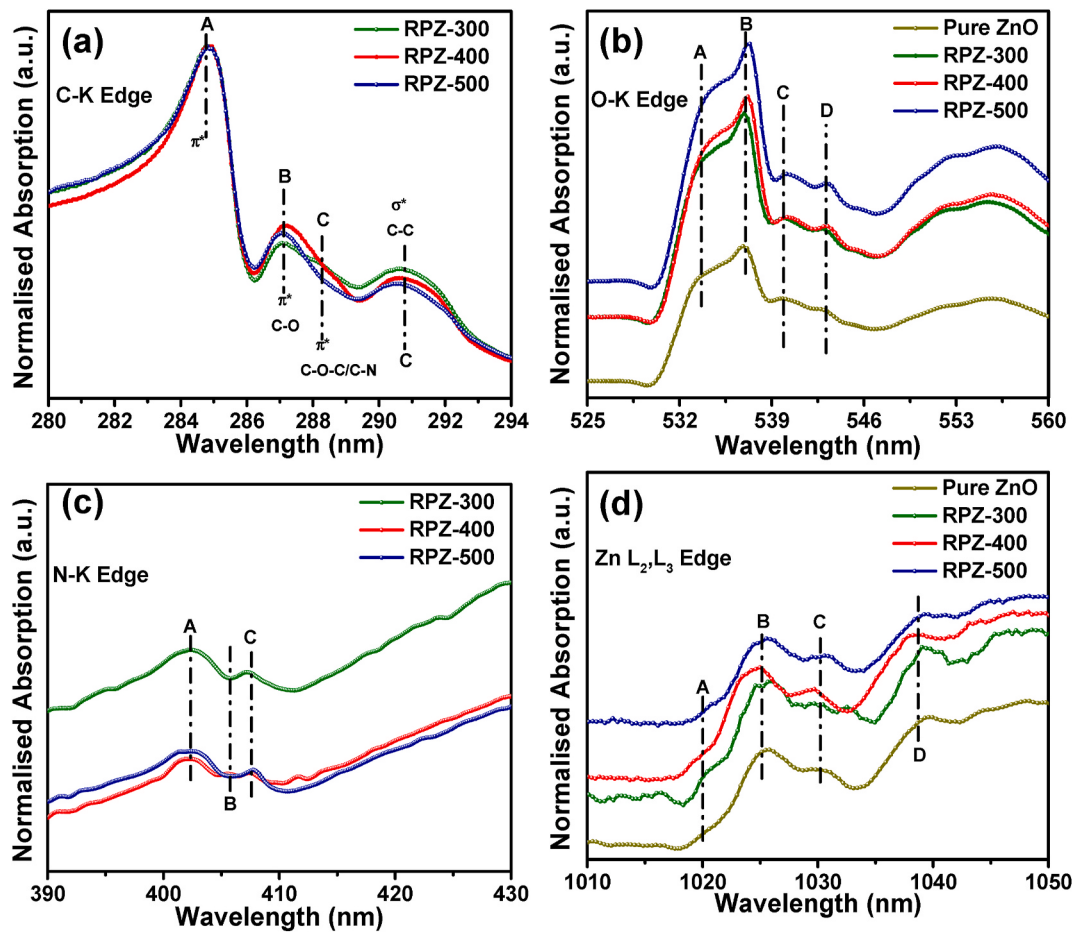


Fig. 4. SXAS spectra of pure ZnO, RPZ-300, RPZ-400, and RPZ-500: (a) C K-edge, (b) O K-edge, (c) N K-edge, and (d) Zn L-edge.

Zn L-edge in SXAS spectra is related to the Zn–O and Zn–C covalent bonds, which further leads to the increase in the charge transfer from O and C 2p states to Zn 4d state [28]. The absorption intensity is directly dependent on the strong overlapping of molecular orbitals with unoccupied states of the neighboring atoms. Moreover, the weak pre-edge absorption is related to the distorted crystalline structure due to a weak interaction with less electronegative atomic orbitals of C. The SXAS results are consistent with the XRD results, further confirming the formation of the RPZ heterojunction nanocomposite.

UV-Vis absorption spectroscopy was performed to analyze the optical absorption properties of pure ZnO, RPZ-300, RPZ-400, and RPZ-500. Each Zn²⁺ (Zn ion) in the wurtzite ZnO structure is surrounded by the four O²⁻ (O ions). The following arrangement gives rise to polar symmetry along the c axis and is called the hexagonal vertical axis. The hybridization between Zn d and O 2p orbitals leads to the formation of an energy bandgap, causing the absorption in the UV-Vis range [24]. Fig. 5 depicts the UV-Vis absorption spectra of the RPZ heterojunction nanocomposites. The absorption peak was observed at 364, 370, 370, and 373 nm for pure ZnO, RPZ-300, RPZ-400, and RPZ-500, respectively. The blue shift in the absorption for the prepared RPZ heterojunction nanocomposite compared to pure ZnO indicates that C was successfully doped in the ZnO structure. Additionally, a broad hump (410–470 nm) was observed for all the RPZ heterojunction nanocomposites which may be caused by the presence of PANI and rGO at the interface [29]. The bandgap energy (E_g) of RPZ heterojunction nanocomposites was calculated using the Tauc plot. Maxima absorption peak was considered for the calculated E_g using the following equation [30]:

$$(\alpha h\nu)^2 = C (h\nu - E_g) \quad (3)$$

where α is the absorption coefficient, h is Planck's constant, ν is the frequency of light, E_g represents the bandgap energy. The inset of Fig. 5 depicts the Tauc plot graphs of pure ZnO and RPZ heterojunction nanocomposites, plotted using the above equation where the extrapolation of the linear part in the graph gives the value of E_g . The calculated E_g values are 3.34, 2.98, 2.98, and 2.80 eV for pure ZnO, RPZ-300, RPZ-400, and RPZ-500, respectively. As expected, the E_g decreased with doping the C. From the graph, with increasing the temperature, the E_g was reduced to 2.80 eV. UV-Vis absorption studies also coincide with the XRD and SXAS results, confirming the formation of the RPZ heterojunction nanocomposite.

UV-Vis absorption studies were performed to investigate the photocatalytic degradation efficiency of the prepared nanocomposites under direct sunlight irradiation against ACP and MB dye. Fig. 6 shows the degradation absorption of (a-c) ACP and (d-f) MB dye with 20 min of time interval in the presence of RPZ heterojunction nanocomposites under direct sunlight. The prominent absorption peaks for ACP and MB dye were obtained at 227 nm [31] and 664 nm [32], respectively, exactly matching with the literature. The absorption spectra show a clear decrease in the prominent absorption peak intensity of both ACP and MB dye as a function of irradiation time. This indicates that the prepared RPZ heterojunction nanocomposite was efficient to degrade the ACP and MB dye in natural sunlight. The degradation efficiency percentage (DF%) and removal efficiency (R%) of catalyst of the nanocomposites for ACP and MB dye were calculated using the following equations [30]:

$$DF\% = (C/C_0) \times 100 \text{ and } R\% = (1-(C/C_0)) \times 100 \quad (4)$$

where C is the concentration at different time intervals, C_0 is the initial

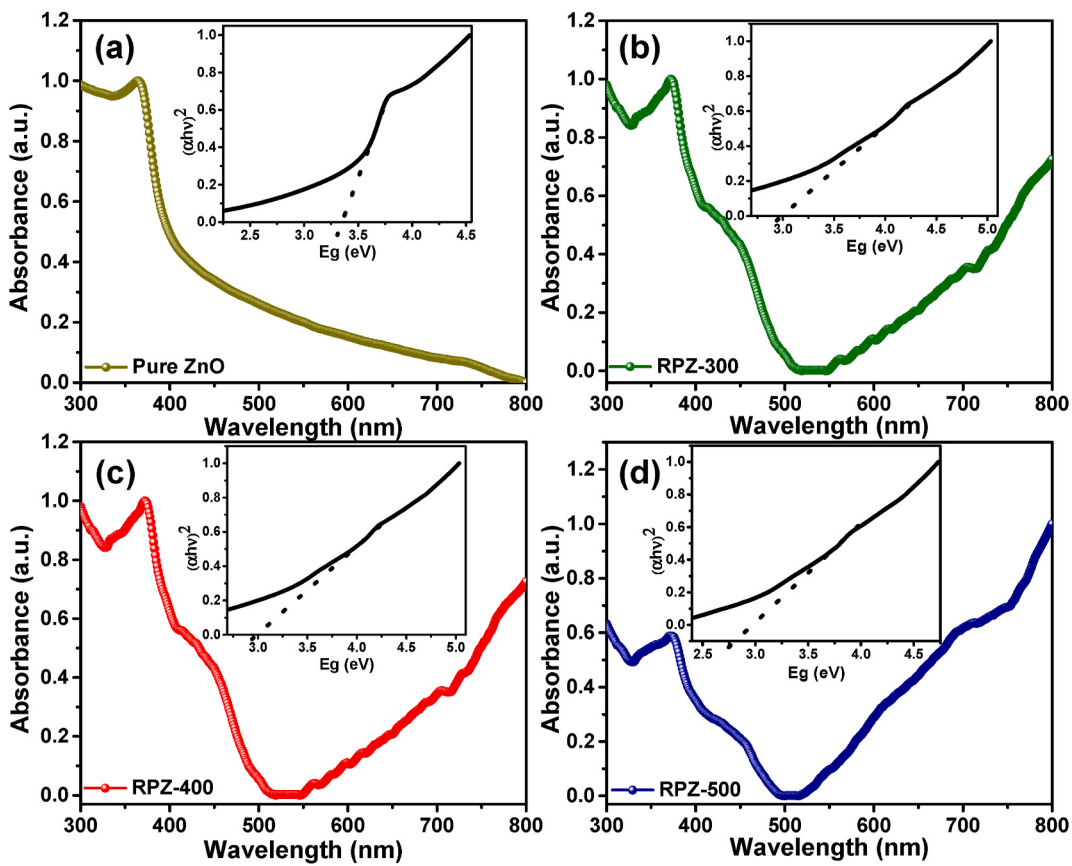


Fig. 5. UV absorption and energy bandgap of (a) pure ZnO, (b) RPZ-300, (c) RPZ-400, and (d) RPZ-500.

concentration. Fig. 7(a)-7(d) shows the DF% and R% of the RPZ-300, RPZ-400, and RPZ-500 nanocomposites for ACP and MB dye as a function of irradiation time. The DF and R% values of the RPZ-300, RPZ-400, and RPZ-500 nanocomposites were 42%, 42%, 47% and 41%, 41%, 46.14% for ACP and 93%, 93%, 95% and 94%, 94%, 95% for MB dye, respectively under direct sunlight irradiation for 100 min. The DF and R % of the nanocomposites were low for ACP compared to MB dye. It is noticeable that using commercially available ACP tablet, the concentration of degradation solution would be relatively very high compared to 10 ppm MB dye solution. Higher degradation efficiency was observed for the RPZ-500 nanocomposite compared to the RPZ-300 and RPZ-400 nanocomposites. This may be due to ZnO annealing temperature because the crystallinity of the ZnO phase in the RPZ-500 nanocomposite was high as compared to the RPZ-300 and RPZ-400 nanocomposites, thus leading to the degradation enhancement in the performance.

The catalytic efficiency of the prepared RPZ heterojunction nanocomposites under direct sunlight was studied, and the obtained degradation results were fit into pseudo-first-order reaction kinetics. The pseudo-first-order reaction kinetic equation is given by the following formula [33]:

$$-\ln(C/C_0) = kt \quad (5)$$

where C is the concentration at different time intervals, C_0 is the initial concentration, k is the rate constant which is equal to the slope of the fitted line. From Fig. 7(e) and (f), it is observable that the photocatalytic degradation process of all the prepared nanocomposites for both ACP and MB dye follows the Hensel Wood pseudo-first-order kinetics. The k values of the RPZ-300, RPZ-400, and RPZ-500 were 0.0052, 0.0043, and 0.0055 min^{-1} for ACP and 0.0242, 0.0253, and 0.0296 min^{-1} for MB dye, respectively. Therefore, the following results reveal that the RPZ-500 nanocomposite exhibits the highest catalytic efficiency for both

ACP and MB dye degradations. A comparison of targeted pollutant, pollutant concentration, light source, catalyst loading, and degradation efficiency is shown in Table 2.

The proposed photocatalytic degradation mechanism of RPZ heterojunction nanocomposites for ACP and MB dye is shown in Fig. 8. The HOMO and LUMO bands of PANI, and the conduction band (CB) and valence band (VB) of ZnO have similar energy levels which may tend to combine and produce the synergistic effect [15]. Since sunlight contains 40% visible light and 10% UV light, to enhance the ZnO activity in the sunlight, the C was doped in ZnO for bandgap narrowing. When sunlight is irradiated on nanocomposite, electron-hole pair is generated, leading to the transport of electrons to CB whereas photo-induced holes remain in VB of ZnO. The well-matching energy level of ZnO VB-PANI HUMO and ZnO CB-PANI LUMO may result in chemical bond interactions, causing the holes in the VB of ZnO to be transferred to the HUMO of PANI [34]. Furthermore, PANI was reported as a good transporter of holes in previous reports [35,36]. Since PANI has a higher negative potential compared to ZnO, photo-generated electrons are transferred to the CB of ZnO [37]. The photo-induced holes diffuse to the surface and breakdown the water molecules into H^+ and OH^- (radicals). Simultaneously, the photo-generated electrons in the ZnO CB band react with O molecules to form superoxide ($\cdot\text{O}_2$). The produced $\cdot\text{O}_2$ and OH^- degrade the ACP and MB dye molecules in water into safe by-products H_2O and CO_2 using redox reactions [38]. Additionally, the presence of the rGO at the interface of the ZnO forms the Schottky barrier. Here, rGO acts as an electron scavenger because ZnO is an n-type semiconductor, and the photo-generated electrons in the ZnO CB freely move to rGO [39]. The purposed mechanism shows enhanced photo-induced charge separation and recombination time by RPZ heterojunction nanocomposite. Moreover, the carboxylic acid functional groups in rGO have strong interaction with PANI and ZnO nanoparticles, resulting in strong adsorption of ZnO and PANI on rGO [15]. ZnO, PANI, and rGO-based photocatalyst

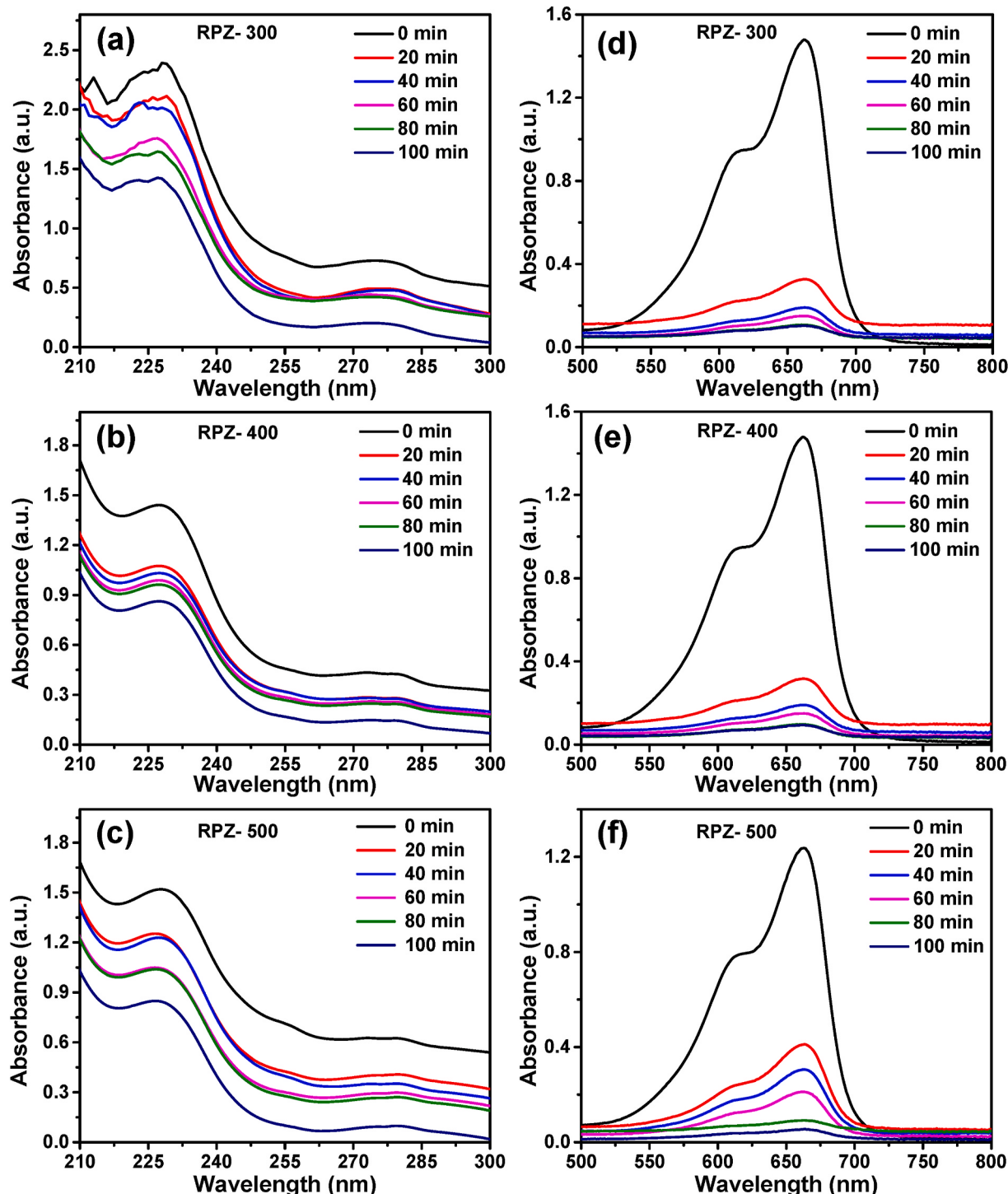
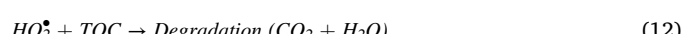
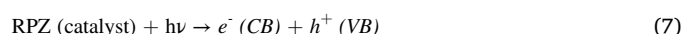


Fig. 6. Photocatalytic degradation of RPZ-300, RPZ-400, and RPZ-500 for (a–c) ACP and (d–f) MB dye, respectively.

materials revealed the excellent long term cyclic stability as reported in previous publications with degradation retention values of 82% by M. A. Ahmed et al. [40], 98% by A. Serrà et al. [41], 97% by S. Huang et al. [42], 90.6% by G. He et al. [43], and 93% by A. Pugazhendhi et al. [44]. The following interaction corresponds to the enhanced long-term cyclic stability of the RPZ nanocomposites. Moreover, ZnO and rGO PANI exhibit antimicrobial properties against *Escherichia coli*, *Vibrio cholerae*, *Staphylococcus epidermidis*, *Salmonella typhi*, *Rhodococcus rhodochrous*, *Proteus mirabilis*, *Staphylococcus aureus*, and *Escherichia fergusonii* [45,46]. The following antimicrobial property further participates in the killing of harmful bacteria present in the water. The surface reactions

occur on the catalyst surface as follows:



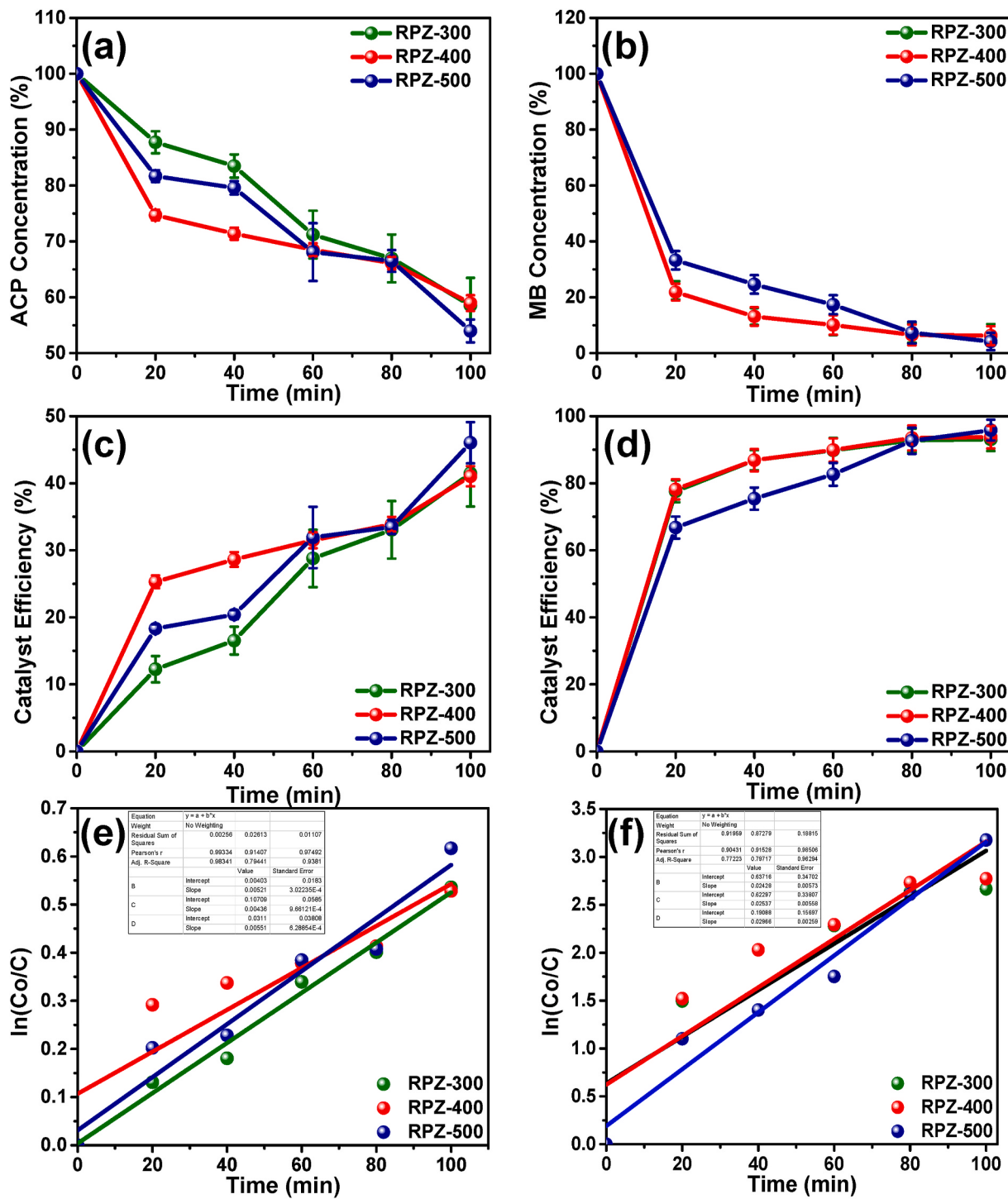


Fig. 7. (a,b) Degradation efficiency percentage (DF%), (c,d) removal efficiency of catalyst (R%), and (e,f) kinetics for ACP and MB dye, respectively.

Table 2

Comparison of various photocatalysts for photocatalytic degradation of MB dye.

Photocatalyst	Targeted pollutant	Pollutant concentration	Light source	Catalyst loading	Degradation efficiency (%)	Reference
PANI-ZnO	MB dye	10 mg/mL	Mercury lamp	50 mg	85.4	[47]
ZnO/rGO	MB dye	10 mg/L	LED light	10 mg	88	[48]
ZnO	MB dye	10 mg/L	LED light	10 mg	84	[48]
CuO/ZnO	MB dye	5 mg/L	Sunlight	20 mg	91	[49]
n-CuO-p-NiO-n-ZnO/rGO	MB dye	—	Visible light	—	70.6	[50]
Cu ₂ O-Cu	MB dye	10 mg/L	Xe lamp	9 mg	90	[51]
Al doped ZnO	MB dye	10 mg/L	Tungsten lamp	80 mg	94	[52]
PANI-rGO-ZnO	MB dye	10 ppm	Natural sunlight	0.1 g	95	Present work

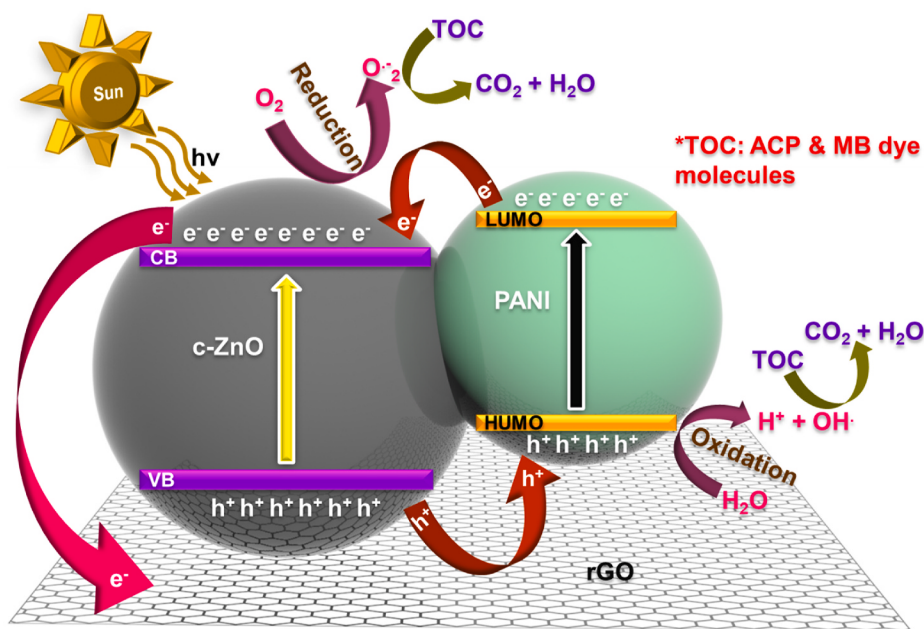


Fig. 8. Schematic representation for the photocatalytic degradation of the RPZ heterojunction nanocomposite for ACP and MB dye molecules.

4. Conclusion

In summary, the RPZ (i.e., rGO and PANI assisted c-ZnO) heterojunction nanocomposites were synthesized successfully. The XRD patterns and SXAS spectra revealed the formation of ternary nanocomposite of rGO, PANI, and ZnO. RPZ nanocomposite exhibited the excellent photocatalytic degradation against ACP and MB dye of 47% and 95% within 100 min under direct natural sunlight with the pseudo-first-order kinetic k values of 0.0055 min^{-1} and 0.0296 min^{-1} , respectively. These results imply that RPZ nanocomposite is expected to have a potential application in photocatalytic pharmaceutical and textile industrial effluent purification.

Declaration of competing interest

The authors declare that they have no known competing financial interests or personal relationships that could have appeared to influence the work reported in this paper.

Acknowledgments

This work was supported by the UGC-DAE Consortium for Scientific Research project with reference numbers CSRIC-BL-48/CRS-165/2016-17/829, 2017-18/786, and CSR-IC/BL-48/CRS-165/2018-19/1421. and special thanks to Dr. Harsimran Singh Bindra for UV analysis. This work was also supported by the National Research Foundation of Korea (NRF) grant funded by the Korean government (MSIP) (2017H1D8A2031138).

References

- [1] J.C. Durán-Álvarez, E. Avella, R.M. Ramírez-Zamora, R. Zanella, Photocatalytic degradation of ciprofloxacin using mono- (Au, Ag and Cu) and bi- (Au-Ag and Au-Cu) metallic nanoparticles supported on TiO₂ under UV-C and simulated sunlight, *Catal. Today* 266 (2016) 175–187.
- [2] M.V. Walter, J.W. Vennes, Occurrence of multiple-antibiotic-resistant enteric bacteria in domestic sewage and oxidation lagoons, *Appl. Environ. Microbiol.* 50 (1985) 930–933.
- [3] R. Alexy, T. Kümpel, K. Kümmeler, Assessment of degradation of 18 antibiotics in the closed bottle test, *Chemosphere* 57 (2004) 505–512.
- [4] H. Wang, G. Zhang, Y. Gao, Photocatalytic degradation of metronidazole in aqueous solution by niobate K₆Nb_{10.8}O₃₀, *Wuhan Univ. J. Nat. Sci.* 15 (2010) 345–349.
- [5] E.S. Elmolla, M. Chaudhuri, Photocatalytic degradation of amoxicillin, ampicillin and cloxacillin antibiotics in aqueous solution using UV/TiO₂ and UV/H₂O₂/TiO₂ photocatalysis, *Desalination* 252 (2010) 46–52.
- [6] R.S. Dariani, A. Esmaili, A. Mortezaali, S. Dehghanpour, Photocatalytic reaction and degradation of methylene blue on TiO₂ nano-sized particles, *Optik* 127 (2016) 7143–7154.
- [7] J. Kaur, S. Bansal, S. Singhal, Photocatalytic degradation of methyl orange using ZnO nanopowders synthesized via thermal decomposition of oxalate precursor method, *Phys. B Condens. Matter* 416 (2013) 33–38.
- [8] P. Gholami, L. Dinipazoh, A. Khataee, Y. Orooji, Sonocatalytic activity of biochar-supported ZnO nanorods in degradation of gemifloxacin: synergy study, effect of parameters and phytotoxicity evaluation, *Ultrason. Sonochem.* 55 (2019) 44–56.
- [9] M. Ghasemi, A. Khataee, P. Gholami, R.D.C. Soltani, A. Hassani, Y. Orooji, In-situ electro-generation and activation of hydrogen peroxide using a CuFeNLDH-CNTs modified graphite cathode for degradation of cefazolin, *J. Environ. Manag.* 267 (2020) 110629.
- [10] R. Hassandoost, S.R. Pouran, A. Khataee, Y. Orooji, S.W. Joo, Hierarchically structured ternary heterojunctions based on Ce³⁺/Ce⁴⁺ modified Fe₃O₄ nanoparticles anchored onto graphene oxide sheets as magnetic visible-light-active photocatalysts for decontamination of oxytetracycline, *J. Hazard Mater.* 376 (2019) 200–211.
- [11] Y. Orooji, M. Ghanbari, O. Amiri, M. Salavati-Niasari, Facile fabrication of silver iodide/graphitic carbon nitride nanocomposites by notable photo-catalytic performance through sunlight and antimicrobial activity, *J. Hazard Mater.* 389 (2020) 122079.
- [12] Y. Orooji, R. Mohassel, O. Amiri, A. Sobhani, M. Salavati-Niasari, Gd₂ZnMnO₆/ZnO nanocomposites: green sol-gel auto-combustion synthesis, characterization and photocatalytic degradation of different dye pollutants in water, *J. Alloys Compd.* 835 (2020) 155240.
- [13] P. Mehdizadeh, Y. Orooji, O. Amiri, M. Salavati-Niasari, H. Moayedi, Green synthesis using cherry and orange juice and characterization of TbFeO₃ ceramic nanostructures and their application as photocatalysts under UV light for removal of organic dyes in water, *J. Clean. Prod.* 252 (2020) 119765.
- [14] I. Karuppasamy, M.S. Samuel, E. Selvarajan, S. Shanmugam, P. Sahaya Murphine Kumar, K. Brindha Devi, A. Pugazhendhi, Ultrasound-assisted synthesis of mixed calcium magnesium oxide (CaMgO₂) nanoflakes for photocatalytic degradation of methylene blue, *J. Colloid Interface Sci.* 584 (2021) 770–778.
- [15] H. Wu, S. Lin, C. Chen, W. Liang, X. Liu, H. Yang, A new ZnO/rGO/polyaniline ternary nanocomposite as photocatalyst with improved photocatalytic activity, *Mater. Res. Bull.* 83 (2016) 434–441.
- [16] P.V. Kamat, Graphene-based nanoarchitectures. Anchoring semiconductor and metal nanoparticles on a two-dimensional carbon support, *J. Phys. Chem. Lett.* 1 (2010) 520–527.
- [17] S. Ghosh, B. Sanjeev, M. Gupta, A.B.V.K. Kumar, XAS studies of brain-sponge CNClZnO nanostructures using polyaniline as dual source for solar light photocatalysis, *Ceram. Int.* 45 (2019) 1314–1321.
- [18] G. Qin, H. Zhang, H. Liao, Z. Li, J. Tian, Y. Lin, D. Zhang, Q. Wu, Novel graphene nanosheet-wrapped polyaniline rectangular-like nanotubes for flexible all-solid-state supercapacitors, *J. Mater. Sci.* 52 (2017) 10981–10992.

- [19] S. Bhadra, D. Khastgir, Determination of crystal structure of polyaniline and substituted polyanilines through powder X-ray diffraction analysis, *Polym. Test.* 27 (2008) 851–857.
- [20] B. Gupta, N. Kumar, K. Panda, V. Kanan, S. Joshi, I. Visoly-Fisher, Role of oxygen functional groups in reduced graphene oxide for lubrication, *Sci. Rep.* 7 (2017) 1–14.
- [21] P. Bindu, S. Thomas, Estimation of lattice strain in ZnO nanoparticles: X-ray peak profile analysis, *J. Theor. Appl. Phys.* 8 (2014) 123–134.
- [22] Y. Zhang, J. Zhou, X. Chen, Q. Feng, W. Cai, MOF-derived C-doped ZnO composites for enhanced photocatalytic performance under visible light, *J. Alloys Compd.* 777 (2019) 109–118.
- [23] O. Game, U. Singh, A.A. Gupta, A. Suryawanshi, A. Banpurkar, S. Ogale, Concurrent synthetic control of dopant (nitrogen) and defect complexes to realize broadband (UV-650 nm) absorption in ZnO nanorods for superior photoelectrochemical performance, *J. Mater. Chem.* 22 (2012) 17302–17310.
- [24] A.B.V.K. Kumar, S. Billa, E.G. Shankar, M.C.S. Subha, C, N dual-doped ZnO nanofoams: a potential antimicrobial agent, an efficient visible light photocatalyst and SXAS studies, *J. Synchrotron Radiat.* 27 (2020) 90–99.
- [25] Z. Wang, L. Wu, J. Zhou, Z. Jiang, B. Shen, Chemoslectivity-induced multiple interfaces in MWCNT/Fe₃O₄@ZnO heterotrimers for whole X-band microwave absorption, *Nanoscale* 6 (2014) 12298–12302.
- [26] Y. Liang, Y. Li, H. Wang, J. Zhou, J. Wang, T. Regier, H. Dai, Co₃O₄ nanocrystals on graphene as a synergistic catalyst for oxygen reduction reaction, *Nat. Mater.* 10 (2011) 780–786.
- [27] J.W. Chiou, J.C. Jan, H.M. Tsai, C.W. Bao, W.F. Pong, M.H. Tsai, I.H. Hong, R. Klauser, J.F. Lee, J.J. Wu, S.C. Liu, Electronic structure of ZnO nanorods studied by angle-dependent X-ray absorption spectroscopy and scanning photoelectron microscopy, *Appl. Phys. Lett.* 84 (2004) 3462–3464.
- [28] J.M. Byrne, V.S. Coker, E. Cespedes, P.L. Wincott, D.J. Vaughan, R.A.D. Pattrick, G. Van Der Laan, E. Arenholz, F. Tuna, M. Bencsik, J.R. Lloyd, N.D. Telling, Biosynthesis of zinc substituted magnetite nanoparticles with enhanced magnetic properties, *Adv. Funct. Mater.* 24 (2014) 2518–2529.
- [29] A. Di Mauro, M. Cantarella, G. Nicotra, G. Pellegrino, A. Gulino, M.V. Brundo, V. Privitera, G. Impellizzeri, Novel synthesis of ZnO/PMMA nanocomposites for photocatalytic applications, *Sci. Rep.* 7 (2017) 1–12.
- [30] D. Tu, H. Liao, Q. Deng, X. Liu, R. Shang, X. Zhang, Renewable biomass derived porous BCN nanosheets and their adsorption and photocatalytic activities for the decontamination of organic pollutants, *RSC Adv.* 8 (2018) 21905–21914.
- [31] D. Sulton, D. Pagan-Rodriguez, X. Zhou, Y. Liu, A.M. Hujer, C.R. Bethel, M. S. Helfand, J.M. Thomson, V.E. Anderson, J.D. Buynak, L.M. Ng, R.A. Bonomo, Clavulanic acid inactivation of SHV-1 and the inhibitor-resistant S130G SHV-1 β-lactamase: insights into the mechanism of inhibition, *J. Biol. Chem.* 280 (2005) 35528–35536.
- [32] V.P. Dinh, T.D.T. Huynh, H.M. Le, V.D. Nguyen, V.A. Dao, N.Q. Hung, L.A. Tuyen, S. Lee, J. Yi, T.D. Nguyen, L.V. Tan, Insight into the adsorption mechanisms of methylene blue and chromium(III) from aqueous solution onto pomelo fruit peel, *RSC Adv.* 9 (2019) 25847–25860.
- [33] Q. Wang, J. Lian, Q. Ma, Y. Bai, J. Tong, J. Zhong, R. Wang, H. Huang, B. Su, Photodegradation of Rhodamine B over a novel photocatalyst of feather keratin decorated CdS under visible light irradiation, *New J. Chem.* 39 (2015) 7112–7119.
- [34] H. Zhang, R. Zong, Y. Zhu, Photocorrosion inhibition and photoactivity enhancement for zinc oxide via hybridization with monolayer polyaniline, *J. Phys. Chem. C* 113 (2009) 4605–4611.
- [35] E.T. Kang, K.G. Neoh, K.L. Tan, Polyaniline: a polymer with many interesting intrinsic redox states, *Prog. Polym. Sci.* 23 (1998) 277–324.
- [36] Y. Shirota, H. Kageyama, Charge carrier transporting molecular materials and their applications in devices, *Chem. Rev.* 107 (2007) 953–1010.
- [37] X. Xu, R. Liu, Y. Cui, X. Liang, C. Lei, S. Meng, Y. Ma, Z. Lei, Z. Yang, PANI/FeUiO-66 nanohybrids with enhanced visible-light promoted photocatalytic activity for the selectively aerobic oxidation of aromatic alcohols, *Appl. Catal. B Environ.* 210 (2017) 484–494.
- [38] N.K. Gupta, Y. Ghaffari, S. Kim, J. Bae, K.S. Kim, M. Saifuddin, Photocatalytic degradation of organic pollutants over MFe₂O₄ (M = Co, Ni, Cu, Zn) nanoparticles at neutral pH, *Sci. Rep.* 10 (2020) 1–11.
- [39] S.M. Lam, J.C. Sin, A.Z. Abdullah, A.R. Mohamed, Photocatalytic TiO₂/carbon nanotube nanocomposites for environmental applications: an overview and recent developments, *Fullerenes Nanotub. Carbon Nanostructures* 22 (2014) 471–509.
- [40] F.A. Fouad, M.A. Ahmed, M.S. Antonious, M.F. Abdel-Messih, Synthesis of an efficient, stable and recyclable AgVO₃/ZnO nanocomposites with mixed crystalline phases for photocatalytic removal of rhodamine B dye, *J. Mater. Sci. Mater. Electron.* 31 (2020) 12355–12371.
- [41] A. Serrà, L. Philippe, Simple and scalable fabrication of hairy ZnO@ZnS core@shell Cu cables for continuous sunlight-driven photocatalytic water remediation, *Chem. Eng. J.* 401 (2020) 126164.
- [42] X. Zhao, S. Huang, Y. Liu, Q. Liu, Y. Zhang, In situ preparation of highly stable polyaniline/W₁₈O₄₉ hybrid nanocomposite as efficient visible light photocatalyst for aqueous Cr(VI) reduction, *J. Hazard Mater.* 353 (2018) 466–475.
- [43] Y. Lei, J. Ding, P. Yu, G. He, Y. Chen, H. Chen, Low-temperature preparation of magnetically separable Fe₃O₄@ZnO-RGO for high-performance removal of methylene blue in visible light, *J. Alloys Compd.* 821 (2020) 153366.
- [44] M.S. Samuel, S. Suman, Venkateshkannan, E. Selvarajan, T. Mathimani, A. Pugazhendhi, Immobilization of Cu₃(btc)₂ on graphene oxide-chitosan hybrid composite for the adsorption and photocatalytic degradation of methylene blue, *J. Photochem. Photobiol. B Biol.* 204 (2020) 111809.
- [45] R. Shanmuganathan, G. Sathishkumar, K. Brindhadevi, A. Pugazhendhi, Fabrication of naringenin functionalized-Ag/RGO nanocomposites for potential bactericidal effects, *J. Mater. Res. Technol.* 9 (2020) 7013–7019.
- [46] A.B.V.K. Kumar, E.S. Saila, P. Narang, M. Aishwarya, M. Gautam, E.G. Shankar, Biofunctionalization and biological synthesis of the ZnO nanoparticles: the effect of Raphanus sativus (white radish) root extract on antimicrobial activity against MDR strain for wound healing applications, *Inorg. Chem. Commun.* 100 (2018) 101–106.
- [47] J. Zhu, C. Shao, X. Li, C. Han, S. Yang, J. Ma, X. Li, Y. Liu, Immobilization of ZnO/polyaniline heterojunction on electrospun polyacrylonitrile nanofibers and enhanced photocatalytic activity, *Mater. Chem. Phys.* 214 (2018) 507–515.
- [48] R. Yousefi, J. Beheshtian, S.M. Seyed-Talebi, H.R. Azimi, F. Jamali-Sheini, Experimental and theoretical study of enhanced photocatalytic activity of Mg-doped ZnO NPs and ZnO/rGO nanocomposites, *Chem. Asian J.* 13 (2018) 194–203.
- [49] A.A.M. Sakib, S.M. Masum, J. Hoinkis, R. Islam, M.A.I. Molla, Synthesis of CuO/ZnO nanocomposites and their application in photodegradation of toxic textile dye, *J. Compos. Sci.* 3 (2019) 91.
- [50] S. Yousaf, T. Kousar, M.B. Taj, P.O. Agboola, I. Shakir, M.F. Warsi, Synthesis and characterization of double heterojunction-graphene nano-hybrids for photocatalytic applications, *Ceram. Int.* 45 (2019) 17806–17817.
- [51] S. Li, Q. Lin, X. Liu, L. Yang, J. Ding, F. Dong, Y. Li, M. Irfan, P. Zhang, Fast photocatalytic degradation of dyes using low-power laser-fabricated Cu₂O-Cu nanocomposites, *RSC Adv.* 8 (2018) 20277–20286.
- [52] H.K. Sharma, R. Archana, R. Sankar ganesh, B.P. Singh, S. Ponnamusamy, Y. Hayakawa, C. Muthamizhchelvan, P. Raji, D.Y. Kim, S.K. Sharma, Substitution of Al³⁺ to Zn²⁺ sites of ZnO enhanced the photocatalytic degradation of methylene blue under irradiation of visible light, *Solid State Sci.* 94 (2019) 45–53.